

# Shape Optimization of Rotating Electric Machines Using Isogeometric Analysis

Melina Merkel , Peter Gangl , and Sebastian Schöps 

**Abstract**—This work deals with shape optimization of electric machines using isogeometric analysis. Isogeometric analysis is particularly well suited for shape optimization as it allows to easily modify the geometry without remeshing the domain. A 6-pole interior permanent magnet synchronous machine (IPMSM) is modeled using a multipatch isogeometric approach and rotation of the machine is realized by modeling the stator and rotor domain separately and coupling them at the interface using harmonic basis functions. Shape sensitivity analysis is used to find the shape derivative of the optimization goal functional, i.e., the total harmonic distortion of the electromotive force. This method allows for a freeform shape optimization which is not restricted by a choice of a set of optimization parameters. This freeform shape optimization is applied for the first time to an isogeometric model of an IPMSM minimizing the total harmonic distortion of the electromotive force as a goal functional, where a reduction of 75 % is achieved.

**Index Terms**—Electric machines, isogeometric analysis, shape optimization.

## I. INTRODUCTION

AS a result of the energy transition, the simulation of electromechanical energy converters, in particular electric machines, is becoming increasingly important to obtain efficient and robust designs. Commonly, a workflow based on analytical estimates and the Finite Element Method (FEM) is used for 2D and finally 3D domains. In most classical approaches, the geometry is only approximated, e.g., with an accuracy that depends on the mesh refinement. These errors can be avoided when using Isogeometric Analysis (IGA) [1]–[4] which uses B-splines and/or Non-Uniform Rational B-splines (NURBS) as basis for geometry and solution space. In IGA, the geometry can be easily and smoothly transformed by moving the control points

Manuscript received March 18, 2020; revised July 4, 2020, September 28, 2020, and December 23, 2020; accepted February 6, 2021. Date of publication February 23, 2021; date of current version November 23, 2021. This work was supported by the German BMBF by the PASIROM Project under Grant 05M2018RDA, the “Excellence Initiative” of the German Federal and State Governments and by the Graduate School of Computational Engineering at Technische Universität Darmstadt. Paper no. TEC-00285-2020. (*Corresponding author: Melina Merkel.*)

Melina Merkel and Sebastian Schöps are with the Institut für Teilchenbeschleunigung und Elektromagnetische Felder (TEMF), Technische Universität Darmstadt, 64289 Darmstadt, Germany, and also with the Centre for Computational Engineering, Technische Universität Darmstadt, 64289 Darmstadt, Germany (e-mail: melina.merkel@tu-darmstadt.de; sebastian.schoeps@tu-darmstadt.de).

Peter Gangl is with the Institut für Angewandte Mathematik, Technische Universität Graz, 8010 Graz, Austria (e-mail: gangl@math.tugraz.at).

Color versions of one or more figures in this article are available at <https://doi.org/10.1109/TEC.2021.3061271>.

Digital Object Identifier 10.1109/TEC.2021.3061271

of the splines such that there is no need to remesh the domain when the geometry is modified. This makes IGA very well suited for shape optimization [5]. Numerical optimization based on magnetic equivalent circuits or finite element models has led to large improvements in the designs of technical applications, e.g., of permanent magnet synchronous machines. During the last 30 years there has been a lot of research on finite element based optimization methods (see, e.g., [6], [7] and the references therein). Originally, mainly gradient-based optimization methods were used (see, e.g., [8]–[10]) but stochastic optimization algorithms became more popular during the last 20 years (see, e.g., [11], [12]). Most of the proposed algorithms use stochastic or population-based optimization, e.g., genetic algorithms and particle swarm optimization (see, e.g., [13]) which have also been extended to multi-objective optimization problems (see, e.g., [14], [15]). For permanent magnet synchronous machines, stochastic optimization methods are commonly used (see, e.g., [16]–[18]).

Recently, promising results have been achieved for the design optimization of electric machines for single and multi-objective optimization problems (see, e.g., [19]–[21]). These works use parameter based optimization methods to improve the design and behavior of the machines.

This contribution deals for the first time with freeform shape optimization of a rotating electrical machine discretized with IGA. We use methods from shape calculus to perform shape sensitivity analysis and obtain the so-called shape derivative. The shape derivative represents the local sensitivity of the functional with respect to changes of the geometry and makes gradient-based optimization feasible. The rotor and stator domains are discretized separately and are coupled using harmonic stator-rotor coupling [22].

The paper is structured as follows: In Section II the model of the electric machine and its quantities of interest are introduced. We introduce the shape optimization problem and derive the formula of the shape derivative using shape calculus in Section III. In Section IV the discretization of the machine and isogeometric analysis are explained. We conclude the paper by explaining our gradient-based shape optimization algorithm and present numerical results for the minimization of the total harmonic distortion of the electromotive force in Section V.

## II. MODEL OF THE ELECTRIC MACHINE

Electromagnetic phenomena are described by Maxwell’s equations. For many applications it is sufficient to consider the

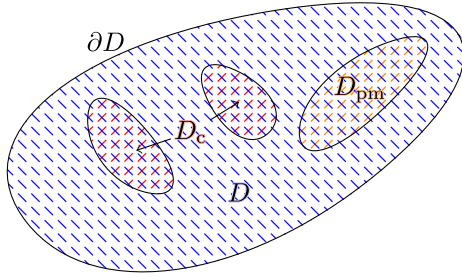


Fig. 1. Example for a domain  $D$  with coil region  $D_c$ , permanent magnet region  $D_{pm}$  and domain boundary  $\partial D$ .

magnetostatic approximation in a working point, i.e., neglecting displacement and eddy currents and nonlinearity of the material laws. In a domain  $D_{3D}$  the magnetostatic formulation of Maxwell's equations is given by

$$\nabla \times (\nu \nabla \times \mathbf{A}) = \mathbf{J}_{src} + \nabla \times \mathbf{M}, \quad (1)$$

with the piecewise constant reluctivity  $\nu$ , the magnetic vector potential  $\mathbf{A}$ , the current density  $\mathbf{J}_{src} = \sum_n \chi_n i_n$  given by winding functions  $\chi_n$  and currents  $i_n$  of the  $n$ -th phase [23], the magnetization of the permanent magnets  $\mathbf{M}$  and homogeneous Dirichlet boundary conditions  $\mathbf{A} \times \mathbf{n} = 0$  on  $\partial D_{3D}$ , where  $\mathbf{n}$  is the normal vector. The source current density  $\mathbf{J}_{src}$  and the permanent magnetization  $\mathbf{M}$  vanish outside the coil ( $D_c$ ) and permanent magnet ( $D_{pm}$ ) regions, respectively, see Fig. 1.

A common quantity of interest when designing electric machines is the total harmonic distortion (THD) of the electromotive force (EMF)  $\mathcal{E}$ .

The EMF of the  $n$ -th phase is defined as the voltage

$$\mathcal{E}_n(\mathbf{A}(t)) = \partial_t \Psi_n(\mathbf{A}(t)), \quad (2)$$

with the flux linkage

$$\Psi_n(\mathbf{A}(t)) = N_p \int_{D_{3D}} \chi_n \cdot \mathbf{A}(t) \, dD_{3D}, \quad (3)$$

where  $N_p$  is the number of pole pairs. The voltage  $\mathcal{E}_n$  are induced by the electromagnetic force in the windings under the assumption that the coils of the poles are connected in series.

The total harmonic distortion of a function  $\mathcal{E} = \mathcal{E}(t)$  is defined as

$$\text{THD}_{\mathcal{I}}(\mathcal{E}) = \frac{\sqrt{\sum_{k \in \mathcal{I}, k \neq 1} |c_k|^2}}{|c_1|}, \quad (4)$$

where  $c_k$  are the coefficients of the Fourier series of  $\mathcal{E}(t)$ , i.e.,

$$\mathcal{E}(t) = \sum_{k=-\infty}^{\infty} c_k e^{ikt}, \quad (5)$$

and  $\mathcal{I} \subset \mathbb{N}$  is an index set of frequencies to consider, e.g., one may disregard frequencies that cannot be diminished by shape optimization. Alternatively, the expansion (5) can be written as

$$\mathcal{E}(t) = \frac{A_0}{2} + \sum_{k=1}^{\infty} A_k \cos(kt) + B_k \sin(kt)$$

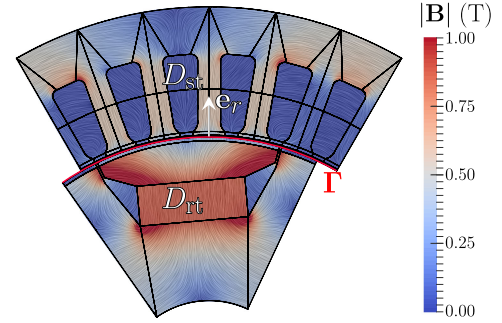


Fig. 2. Multipatch model of one pole of a 6-pole interior permanent magnet synchronous machine. The magnetic flux density  $\mathbf{B}$  is shown which is computed under no load condition using isogeometric analysis.

with coefficients  $A_k = c_k + c_{-k}$  for  $k \geq 0$  and  $B_k = \iota(c_k - c_{-k})$  for  $k \geq 1$ . Note that it holds that  $|c_k| = \sqrt{A_k^2 + B_k^2}/2$ . Using these coefficients, the THD can be written as

$$\text{THD}(\mathcal{E}) = \sqrt{\frac{\sum_{k \in \mathcal{I}, k \neq 1} A_k^2 + B_k^2}{A_1^2 + B_1^2}}. \quad (6)$$

As we are interested in the THD of the EMF we need to consider (6) for the voltages (2). Therefore, the amplitudes  $c_k$  in (4) or  $A_k$  and  $B_k$  in (6) are obtained by Fourier analysis of the voltages.

In the planar 2D case (1) is considered on a cross section  $D \subset \mathbb{R}^2$  and reduces to

$$-\nabla \cdot (\nu \nabla u) = J_{src,z} + \nabla \times \mathbf{M} \cdot \mathbf{e}_z, \quad (7)$$

where  $u(x, y)$  is the  $z$ -component of the magnetic vector potential  $\mathbf{A} = [0, 0, u]^\top$ ,  $J_{src,z} = \sum_n \chi_n i_n$  is the  $z$ -component of the current density given by winding functions  $\chi_n$  and currents  $i_n$  of the  $n$ -th phase and  $\mathbf{e}_z$  is the unit vector in  $z$ -direction.

### III. OPTIMIZATION

#### A. Problem Statement

We want to optimize the 2D shape  $\Omega$  of the 3-phase interior permanent magnet synchronous machine (IPMSM) from Fig. 2, which has  $N_p = 3$  pole pairs, in terms of the total harmonic distortion (THD) of the electromotive force (EMF) as introduced in (2). Due to periodicity of the stator windings, we will restrict ourselves to the optimization of the first voltage and set  $\mathcal{E} := \mathcal{E}_1$  and  $\chi = \chi_1$ . Note the dependence of  $\mathcal{E}$  on the shape  $\Omega$  via the solution  $u$  to (7), i.e.,  $\mathcal{E} = \mathcal{E}(u(t, \Omega))$ . Thus, we consider the optimization problem

$$\min_{\Omega \in \mathcal{A}} \mathcal{J}(\Omega) := \text{THD}_{\mathcal{I}}(\mathcal{E}(u(t, \Omega))), \quad (8)$$

$$\text{s.t. } c(\Omega) = 0, \quad (9)$$

where  $c(\Omega)$  are physical constraints and the optimization problem (8)–(9) is constrained by the machine model (7), which, for  $t \in [0, T]$ , reads in its weak form: Find  $u = u(\alpha(t))$  such that

$$\int_D \underbrace{\nu_\Omega(\alpha(t)) \nabla u \cdot \nabla v \, dD}_{=: a[\alpha(t)](\Omega; u, v)} = \langle r(t, \alpha(t)), v \rangle \quad (10)$$

for all test functions  $v$ . Here  $T = 2\pi/\omega$  is the (electrical) period length,  $\alpha(t)$  the rotor angle, which may be given by the equation of motion. We allow all geometries from an admissible set  $\mathcal{A}$ . Both  $u$  and  $v$  satisfy homogeneous Dirichlet boundary conditions on the inner and outer circular parts of the boundary and periodic boundary conditions on the left and right parts of the boundary. Finally, the right-hand-side is given by

$$\begin{aligned} \langle r(t, \alpha(t)), v \rangle &= \int_{D_c} \sum_{k=1}^3 \chi_k(x, y) i_k(t) v(x, y) \, dD_c \\ &+ \int_{D_{\text{pm}}(\alpha(t))} \begin{pmatrix} -M_2 \\ M_1 \end{pmatrix} \cdot \nabla v(x, y) \, dD_{\text{pm}}(\alpha(t)) \end{aligned} \quad (11)$$

and contains the excitations due to permanent magnets and the coils. Here,  $M_1$  and  $M_2$  are the first and second component of the magnetization vector  $\mathbf{M}$ , respectively,  $D_{\text{pm}}(\alpha(t))$  denotes the permanent magnet region after rotation by the angle  $\alpha(t)$  and we exploit for a more compact notation that the permanent magnets lie in the rotating part and the coils in the stator. We indicate the dependence of the reluctivity function on the current shape  $\Omega$  which is subject to the shape optimization by writing  $\nu_\Omega$ .

Moreover, we introduce a temporal discretization  $\{t_1, \dots, t_{N_\alpha}\}$  into  $N_\alpha$  points in time and a corresponding discretization of the range of angular displacements into  $N_\alpha$  rotor positions,  $\boldsymbol{\alpha} := (\alpha_1, \dots, \alpha_{N_\alpha})$ . For  $j \in \{1, \dots, N_\alpha\}$  and a given shape  $\Omega$ , let  $a_j(\Omega; \cdot, \cdot) := a[\alpha_j](\Omega; \cdot, \cdot)$  and  $r_j := r(t_j, \alpha_j)$  according to the definitions in (10) and (11), respectively. Approximating  $u(t, \Omega)$  for  $t \in [0, T]$  by  $\{u_1, \dots, u_{N_\alpha}\}$  and introducing the notation  $\mathcal{J}(u_1, \dots, u_{N_\alpha}) := \text{THD}_T(\mathcal{E}(u_1, \dots, u_{N_\alpha}))$ , problem (8)–(10) after discretization with respect to rotor positions can be written as the optimization problem

$$\min_{\Omega} \mathcal{J}(u_1, \dots, u_{N_\alpha}) \quad (12)$$

$$\begin{cases} a_1(\Omega; u_1, v_1) = \langle r_1, v_1 \rangle \forall v_1, \\ \vdots \\ a_{N_\alpha}(\Omega; u_{N_\alpha}, v_{N_\alpha}) = \langle r_{N_\alpha}, v_{N_\alpha} \rangle \forall v_{N_\alpha}, \\ c(\Omega) = 0, \end{cases} \quad (13)$$

which is constrained by  $N_\alpha$  boundary value problems corresponding to the  $N_\alpha$  rotor positions under consideration.

### B. Shape Sensitivity Analysis

The shape derivative  $d\mathcal{J}(\Omega; \mathbf{W})$  of a domain-dependent functional  $\mathcal{J} = \mathcal{J}(\Omega)$  represents the sensitivity of the functional with respect to a perturbation of the domain in the direction of a given vector field  $\mathbf{W}$ . The shape derivative is defined as

$$d\mathcal{J}(\Omega; \mathbf{W}) = \lim_{\delta \searrow 0} \frac{\mathcal{J}(T_\delta^{\mathbf{W}}(\Omega)) - \mathcal{J}(\Omega)}{\delta}, \quad (14)$$

if this limit exists and the mapping  $\mathbf{W} \mapsto d\mathcal{J}(\Omega; \mathbf{W})$  is linear and continuous on the space of smooth vector fields. Here,  $T_\delta^{\mathbf{W}}$  represents a transformation which moves every point  $\mathbf{x}$

a distance  $\delta > 0$  in the direction given by the vector field  $\mathbf{W}$ ,  $T_\delta^{\mathbf{W}}(\mathbf{x}) = \mathbf{x} + \delta \mathbf{W}(\mathbf{x})$ .

For deriving the shape derivative  $d\mathcal{J}(\Omega; \mathbf{W})$  for the optimization problem (12)–(13), we follow the steps taken in [24]. First, we introduce the Lagrangian

$$\mathcal{L}(\Omega, \varphi_1, \dots, \varphi_{N_\alpha}, \psi_1, \dots, \psi_{N_\alpha}) :=$$

$$\mathcal{J}(\varphi_1, \dots, \varphi_{N_\alpha}) + \sum_{k=1}^{N_\alpha} (a_k(\varphi_k, \psi_k) - \langle r_k, \psi_k \rangle).$$

For ease of notation, we will use the notation  $\mathbf{u} = (u_1, \dots, u_{N_\alpha})$  and similar for other quantities. Note that, for  $u_i$  satisfying the  $i$ -th equation of (13), it holds that

$$\frac{\partial}{\partial \psi_i} \mathcal{L}(\Omega, \mathbf{u}, \boldsymbol{\psi})(q_i) = a_i(u_i, q_i) - \langle r_i, q_i \rangle = 0$$

for any test function  $q_i$ . Similarly, we introduce the adjoint states  $p_i$ ,  $i = 1, \dots, N_\alpha$ , as the solutions to

$$0 = \frac{\partial}{\partial \varphi_i} \mathcal{L}(\Omega, \mathbf{u}, \mathbf{p})(v_i) = \frac{\partial \mathcal{J}}{\partial \varphi_i}(\mathbf{u})(v_i) + a_i(v_i, p_i) \quad (15)$$

for all test functions  $v_i$ .

Let us now consider the functional  $\mathcal{J} = \mathcal{J}(u_1, \dots, u_{N_\alpha})$  more closely. We will use the representation (6) for the THD. Let  $(C_k)_{k \in \mathcal{I}}$  be the Fourier coefficients of the function  $\Psi(u_1, \dots, u_{N_\alpha})$ , i.e.,

$$\Psi(u_1, \dots, u_{N_\alpha}) = \sum_{k=-[N_\alpha/2]}^{[N_\alpha/2]} C_k e^{ikt}. \quad (16)$$

Using the Fourier representation (16) of the flux linkage and (2), the electromotive force can be written as

$$\mathcal{E}(u_1, \dots, u_{N_\alpha}) = \sum_{k=-[N_\alpha/2]}^{[N_\alpha/2]} \underbrace{ik C_k}_{c_k} e^{ikt}, \quad (17)$$

where  $(c_k)_{k \in \mathcal{I}}$  are the Fourier coefficients of the electromotive force  $\mathcal{E}$ . This Fourier series can be rewritten as

$$\mathcal{E}(u_1, \dots, u_{N_\alpha}) = \frac{A_0}{2} + \sum_{k=1}^{[N_\alpha/2]} A_k \cos(kt) + B_k \sin(kt). \quad (18)$$

The coefficients  $A_k$  and  $B_k$  of the Fourier representation of  $\partial_t \Psi$  (18) are obtained by time derivation and Fourier transform, which we will denote by  $A_k = [\mathcal{F}'_a(\Psi(u_1, \dots, u_{N_\alpha}))]_k$  and  $B_k = [\mathcal{F}'_b(\Psi(u_1, \dots, u_{N_\alpha}))]_k$ , respectively. Exploiting the linearity of the discrete Fourier transform, the vectors  $\mathbf{A}$  and  $\mathbf{B}$  can also be written in terms of transformation matrices  $\mathbf{M}_a = \mathcal{F}'_a(\mathbf{I})$  and  $\mathbf{M}_b = \mathcal{F}'_b(\mathbf{I})$ , where  $\mathbf{I}$  is the identity matrix, i.e.,

$$A_{k-1}(u_1, \dots, u_{N_\alpha}) = \sum_{j=1}^{N_\alpha} \left( (\mathbf{M}_a)_{k,j} N_p l_z \int_D \chi u_j \, dD \right), \quad (19)$$

$$B_{k-1}(u_1, \dots, u_{N_\alpha}) = \sum_{j=1}^{N_\alpha} \left( (\mathbf{M}_b)_{k,j} N_p l_z \int_D \chi u_j \, dD \right), \quad (20)$$

where  $l_z$  is the length of the machine in  $z$ -direction.

In order to solve the adjoint state equation (15), we need to differentiate the functional  $\mathcal{J} = \text{THD}(\mathcal{E}(u_1, \dots, u_{N_\alpha}))$  with respect to  $u_i$  for  $i \in \{1, \dots, N_\alpha\}$ . Using the relation (6), we obtain

$$\begin{aligned} \frac{d \text{THD}(\mathcal{E}(\mathbf{u}))}{du_i}(\mathbf{u})(v_i) = & \\ & \frac{1}{\sqrt{A_1^2 + B_1^2}} \frac{1}{\sqrt{\sum_{k \in \mathcal{I}, k \neq 1} A_k^2 + B_k^2}} \left( \sum_{k \in \mathcal{I}, k \neq 1} A_k A'_k + B_k B'_k \right) \\ & - \frac{1}{(A_1^2 + B_1^2)^{3/2}} \left( \sqrt{\sum_{k \in \mathcal{I}, k \neq 1} A_k^2 + B_k^2} (A_1 A'_1 + B_1 B'_1) \right). \end{aligned}$$

Here, we used the abbreviations  $A'_k := \frac{dA_k}{du_i}(\mathbf{u})(v_i)$  and  $B'_k := \frac{dB_k}{du_i}(\mathbf{u})(v_i)$ . It can be seen from (19) and (20) that

$$\begin{aligned} \frac{dA_k}{du_i}(\mathbf{u})(v_i) &= (\mathbf{M}_a)_{k,i} N_p l_z \int_D \chi v_i \, dD, \\ \frac{dB_k}{du_i}(\mathbf{u})(v_i) &= (\mathbf{M}_b)_{k,i} N_p l_z \int_D \chi v_i \, dD. \end{aligned}$$

Given the solutions to the forward problem (10) for all rotor positions  $l \in \{1, \dots, N_\alpha\}$ , we obtain for the adjoint problem (15) defining the adjoint variable at rotor position  $l \in \{1, \dots, N_\alpha\}$ : Find  $p_i$  such that

$$a_i(v_i, p_i) = - \frac{d \text{THD}(\mathcal{E}(\mathbf{u}))}{du_i}(\mathbf{u})(v_i)$$

for all test functions  $v_i$ .

Finally, in a similar way as it was proposed in [24], assuming that the deformation vector field  $\mathbf{W}$  vanishes on the interface  $\Gamma$  and on the stator, and that the permanent magnet region remains unchanged, we obtain the formula for the shape derivative in the direction of a smooth vector field  $\mathbf{W} \in C^1(D, \mathbb{R}^2)$ :

$$\begin{aligned} d\mathcal{J}(\Omega; \mathbf{W}) &= \sum_{l=1}^{N_\alpha} \int_{D_{\text{pm}}} (\nabla \cdot (\mathbf{W}) \mathbf{I} - \mathbf{D}\mathbf{W}^\top) \nabla p_l \cdot \begin{pmatrix} -M_2 \\ M_1 \end{pmatrix} dx \\ &+ \sum_{l=1}^{N_\alpha} \int_D \nu (\nabla \cdot \mathbf{W} \mathbf{I} - \mathbf{D}\mathbf{W}^\top - \mathbf{D}\mathbf{W}) \nabla u_l \cdot \nabla p_l \, dx. \end{aligned} \quad (21)$$

Here,  $\mathbf{I} \in \mathbb{R}^{2 \times 2}$  denotes the two-dimensional identity matrix.

#### IV. SOLUTION OF THE FORWARD PROBLEM BY IGA

In this section, we will give an overview of Isogeometric Analysis which is used to discretize the forward problem (7) allowing for an exact representation of the machine geometry and straightforward manipulation of the shape. For a flexible treatment of the rotation we model stator and rotor separately and use harmonic stator-rotor coupling for the solution of the discretized problem, obtaining the saddle-point formulation given in [22], [25].

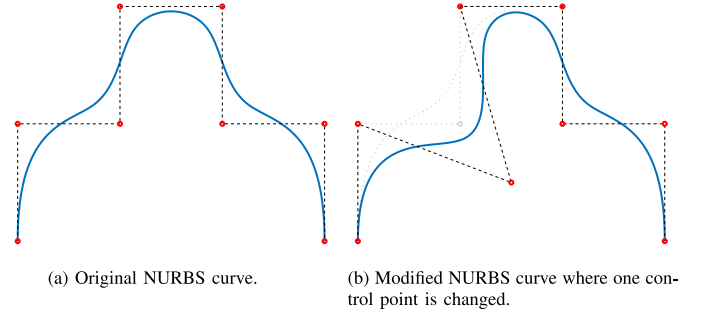


Fig. 3. Visualization of the modification of the shape of a NURBS curve by moving one control point.

#### A. B-Splines and NURBS

Isogeometric analysis is based on the idea of using freeform curves for an exact geometry representation of CAD models. This avoids errors in the geometry induced by mesh generation. For this, the notion of *B-splines*, i.e., piecewise polynomial functions, is of central importance. B-splines are defined via a *knot vector*  $\Xi = \{\xi_1, \xi_2, \dots, \xi_{n+p+1}\}$  where the knots  $\xi_i \in [0, 1]$  for all  $i \in \{1, \dots, n+p+1\}$  are coordinates in the parametric space,  $p$  is the degree of the B-spline and  $n$  will be the dimension of the space. B-splines are defined by the recursive Cox-de Boor formula [26]

$$B_{i,p}(\xi) = \frac{\xi - \xi_i}{\xi_{i+p} - \xi_i} B_{i,p-1}(\xi) + \frac{\xi_{i+p+1} - \xi}{\xi_{i+p+1} - \xi_{i+1}} B_{i+1,p-1}(\xi), \quad (22)$$

for all  $p \geq 1$  and for  $p = 0$  via

$$B_{i,0}(\xi) = \begin{cases} 1 & \text{if } \xi_i \leq \xi < \xi_{i+1}, \\ 0 & \text{else,} \end{cases} \quad (23)$$

where  $0/0 = 0$  is formally assumed. *NURBS* (Non-Uniform Rational B-splines) basis functions are then defined by

$$N_{i,p}(\xi) = \frac{w_i B_{i,p}(\xi)}{\sum_{k=1}^n w_k B_{k,p}(\xi)}, \quad (24)$$

where  $w_k > 0$  for all  $k = 1, 2, \dots, n$  are so-called *weights*. NURBS curves can then be defined by the NURBS basis functions and control points  $\mathbf{P}_i$  as

$$\mathbf{C}(\xi) = \sum_{i=1}^n \mathbf{P}_i N_{i,p}(\xi). \quad (25)$$

A NURBS curve can be locally modified by moving the control points. This is visualized in Fig. 3.

#### B. Isogeometric Analysis

Using the same functions for the representation of the geometry as in CAD software, i.e., NURBS, has the advantage that there is no need for the construction of a finite element geometry, i.e., the mesh. In isogeometric analysis the geometry is represented by a smooth mapping

$$\mathbf{F} : \hat{D} \rightarrow D, \quad (26)$$

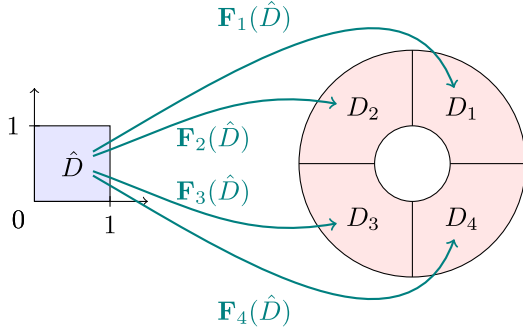


Fig. 4. Visualization of the mappings  $\mathbf{F}_k$  from the reference domain  $\hat{D}$  to the patches  $D_k$  of a multipatch geometry.

using NURBS as basis functions, where  $\hat{D}$  is the reference domain, i.e., in the 2D case the unit square, and  $D$  is the physical domain. The mapping  $\mathbf{F}$  can be directly obtained from CAD software. However, not all geometries can be represented by a regular transformation of the reference domain  $\hat{D} = [0, 1]^n$ , e.g., domains with a hole. In this case, a multipatch approach can be used to represent the physical domain. The physical domain  $D$  is subdivided into  $k$  patches  $D_k$  which can each be represented by a regular transformation of the reference domain  $D_k = \mathbf{F}_k(\hat{D})$ . A visualization is given in Fig. 4. The patches have a consistent discretization with a one-to-one matching of the degrees of freedom at the interfaces as in the classical FEM, leading to a  $C^0$  smoothness of the solution at the patch interfaces. Thus, the geometry of the CAD models can be exactly represented by a multipatch model [27] and there is no need for the generation of a computational mesh that approximates the geometry, e.g., a triangulation. For the analysis, IGA uses the same setting as the classical finite element analysis with the exception of using B-splines or NURBS as basis and test functions  $w_j$  for  $j = 1, \dots, N_q$ .

## V. NUMERICAL SHAPE OPTIMIZATION

We solve the optimization problem (8)–(10) by means of a gradient-based shape optimization algorithm based on the shape derivative (21) where constraints (9) can be incorporated by means of the augmented Lagrangian method [28], [29] where the objective function is augmented by terms involving the constraint  $c(\Omega)$  with suitably updated coefficients. By solving an auxiliary boundary value problem of the form

$$b(\mathbf{W}, \mathbf{Z}) = d\mathcal{J}(\Omega; \mathbf{Z}) \quad \forall \mathbf{Z} \quad (27)$$

with some positive definite bilinear form  $b(\cdot, \cdot)$  satisfying  $b(\mathbf{Z}, \mathbf{Z}) > 0$  for all vector fields  $\mathbf{Z}$ , we can extract a shape gradient  $\mathbf{W}$ , which satisfies  $d\mathcal{J}(\Omega; \mathbf{W}) = b(\mathbf{W}, \mathbf{W}) > 0$ . Thus, moving the control points of the motor geometry a small distance  $\delta$  into the direction of  $\mathbf{W}$  will yield an increase of the objective function  $\mathcal{J}$ . Likewise, since  $d\mathcal{J}(\Omega; \mathbf{W})$  is linear in  $\mathbf{W}$ , a decrease can be achieved by moving the control points into the direction of the negative shape gradient  $-\mathbf{W}$ . The auxiliary boundary value problem (27) can be interpreted as finding a Riesz representative  $\mathbf{W}$  of the functional  $d\mathcal{J}(\Omega, \cdot)$  with respect

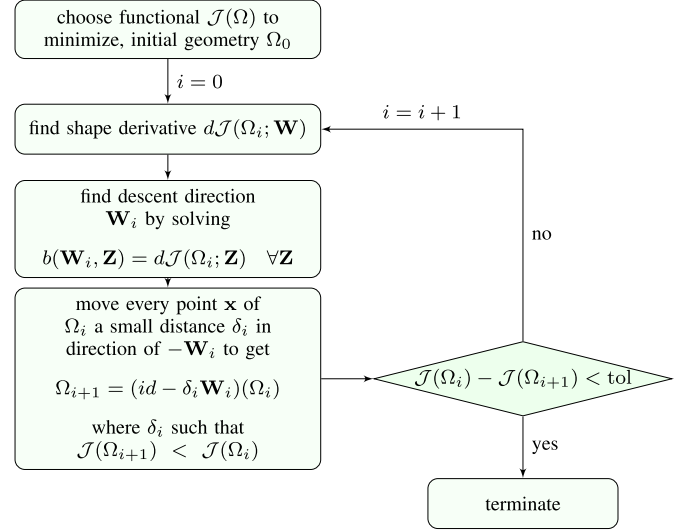


Fig. 5. Overview of the unconstrained shape optimization algorithm.

to the metric given by  $b(\cdot, \cdot)$ . Of course, here different bilinear forms  $b(\cdot, \cdot)$  can be chosen which amount to shape gradients in different metrics. In our algorithm, we choose

$$b(\mathbf{W}, \mathbf{Z}) = \int_D \mathbf{D}\mathbf{W} : \mathbf{D}\mathbf{Z} + \mathbf{W} \cdot \mathbf{Z} \, dx \quad (28)$$

where  $\mathbf{A} : \mathbf{B} = \sum_{i,j=1}^n A_{ij} B_{ij}$  denotes the Frobenius inner product for two matrices  $\mathbf{A}, \mathbf{B} \in \mathbb{R}^n$  and  $\mathbf{D}\mathbf{W}$ ,  $\mathbf{D}\mathbf{Z}$  denote the Jacobians of  $\mathbf{W}$ ,  $\mathbf{Z}$ , respectively. Our algorithm consists in iteratively determining a descent vector field  $\mathbf{W}$  by solving the auxiliary boundary value problem (27) with the bilinear form  $b(\cdot, \cdot)$  given by (28) and moving the domain a distance  $\delta$  into this direction. The step size  $\delta$  is chosen as the maximum of the set  $\{1, 1/2, 1/4, \dots\}$  such that, no intersections of the patches occur and the objective value is decreased. When no further improvement can be achieved, the algorithm terminates. An overview of the shape optimization algorithm is given in Fig. 5.

## VI. OPTIMIZATION RESULTS

The method described in Section V is used to minimize the total harmonic distortion of the electromotive force by shape optimizing the rotor of a 6-pole interior permanent magnet synchronous machine in generator mode under no load condition without additional constraints. This machine is derived from a machine that was originally designed as part of a drive for a tool machine [30, page 124]. The description of geometry and material coefficients can be found in [31, Chapter V.A]. The shape and position of the permanent magnets in the rotor are fixed. The machine is discretized by  $N_{\text{DoF}} = 4354$  degrees of freedom using B-splines of degree  $p = 2$  as basis functions and linearized material laws. The implementation is based on GeoPDEs [32]. The level of refinement is chosen such that the relative error in the  $L^2$ -norm of the magnetic vector potential  $u$  in the domain is smaller than  $10^{-3}$ . The coupling of stator and rotor domain is realized using  $N_{\Gamma} = 36$  harmonic basis functions.

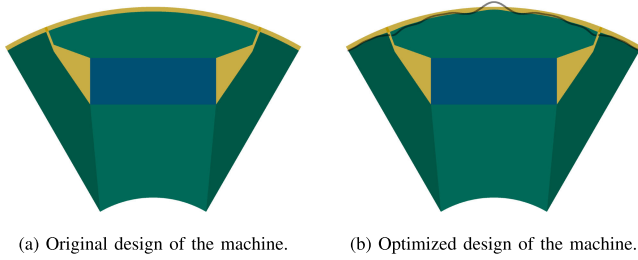


Fig. 6. Results of shape optimization (8) in generator mode under no load condition. The shape of the rotor was optimized, minimizing the total harmonic distortion. Shape and position of the permanent magnet was fixed. The black line shows the changes in the rotor amplified by a factor of 5.

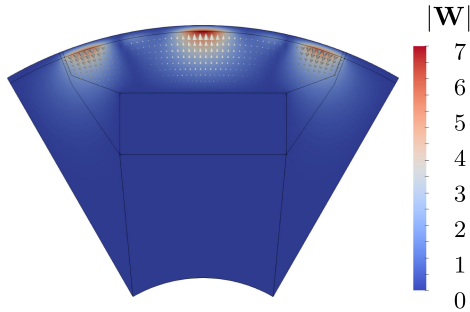


Fig. 7. Magnitude of the shape gradient in the first iteration of the shape optimization algorithm. Arrows indicate the direction of the negative shape gradient.

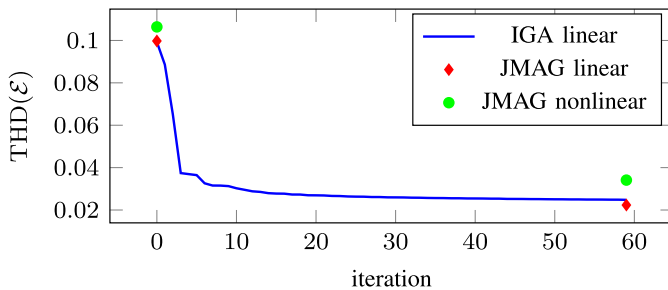
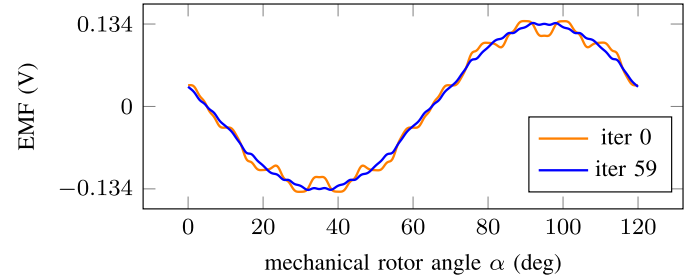
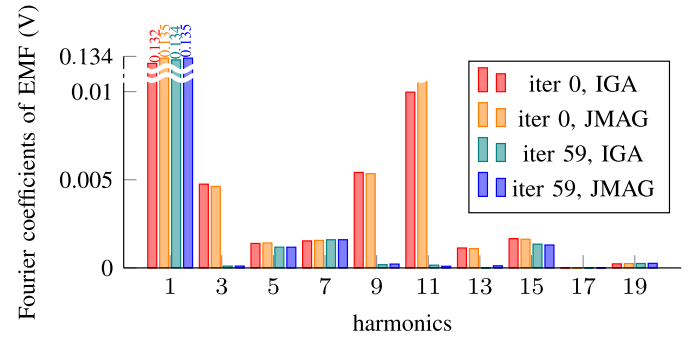


Fig. 8. Total harmonic distortion of the electromotive force  $\mathcal{E}$  for each iteration of the shape optimization (8) in generator mode under no load condition computed with IGA and with JMAG using linear and nonlinear material relations as a reference.

The simulation of a rotation of  $120^\circ$  with  $N_\alpha = 120$  takes about 10 s. The optimization process takes about 2 h and is carried out in MATLAB R2019a on a 6-core machine (Intel Core<sup>TM</sup> i7-5820 K CPU) with 16 GB RAM. The original and optimized design of the rotor can be seen in Fig. 6. The sensitivity, i.e., the shape gradient  $\mathbf{W}$  during the first iteration of the optimization is visualized in Fig. 7. The total harmonic distortion is reduced by more than 75 % in 59 iterations. The total harmonic distortion in the iterations of the shape optimization algorithm and the electromotive force and its Fourier coefficients of the original design compared to the electromotive force and its Fourier coefficients of the optimized design can be seen in Figs. 8, 9.



(a) Electromotive force for a rotation of the rotor.



(b) Fourier coefficients of the electromotive force.

Fig. 9. Electromotive force for the original design and for the optimized design after 59 iterations. Computed using linear material laws.

The machine has also been optimized under full load condition with the physical constraint

$$c(\Omega) = \tau(\Omega) - \tau_{\text{orig}} = 0, \quad (29)$$

where  $\tau(\Omega)$  denotes the average torque for the machine design  $\Omega$  and  $\tau_{\text{orig}}$  denotes the average torque for the original machine. Thus, the average torque is maintained. The constraint (29) is incorporated using the well-known augmented Lagrangian method [28], where the shape derivative of the torque is derived analogously to Section III-B. In this optimization the THD of the EMF is reduced by 44 % while the torque is maintained. The resulting geometry of the rotor is shown in Fig. 12 and the CAD description of the original and optimized machine geometries is available as an IGES file [33].

## VII. VALIDATION

Exploiting the geometry representation which is given directly in NURBS, i.e., the representation commonly used in computer-aided design (CAD), the model can be easily imported into computer-aided-engineering (CAE) software, e.g., using the IGES (Initial Graphics Exchange Specification) format. The results of the optimization in Section VI is validated by using JMAG as reference solution. The JMAG model has 281 198 elements of order 1 and the meshing takes about 15 s. The simulation of a single rotation of  $120^\circ$  with  $N_\alpha = 120$  takes about 30 min. The results of the JMAG simulation using linearized material laws is shown in Figs. 8 and 9. They are in very good agreement with the results from GeOPDEs for both geometries. The main characteristics of the original and optimized motor design are given in Table II. The cogging torque and magnetic

TABLE I  
TOTAL HARMONIC DISTORTION OF THE ELECTROMOTIVE FORCE  $\mathcal{E}$  FOR ORIGINAL AND THE OPTIMIZED ROTOR DESIGN COMPUTED WITH IGA AND WITH JMAG FOR LINEAR AND NONLINEAR MATERIAL LAWS

	THD( $\mathcal{E}$ ) original design	THD( $\mathcal{E}$ ) optimized design
IGA linear	0.099268	0.024793
JMAG linear	0.099754	0.02234
JMAG nonlinear	0.10639	0.034106

TABLE II  
MAIN CHARACTERISTICS OF THE ORIGINAL AND THE OPTIMIZED ROTOR DESIGN COMPUTED WITH JMAG

	original design	optimized design
Rated speed	1930 rpm	1930 rpm
Rated current $I_{\text{eff}}$	10.6 A	10.6 A
Torque $\tau$	11.62 Nm	11.34 Nm
Power $P$	2349.0 W	2292.1 W
Open circuit voltage $\mathcal{E}$	57.76 V	57.72 V
Flux linkage $\Psi$	0.0953 Wb	0.0952 Wb

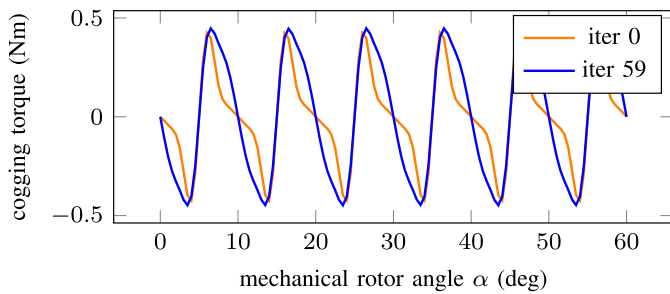


Fig. 10. Cogging torque of the motor for the original design and for the optimized design after 59 iterations. Computed using linear material laws.

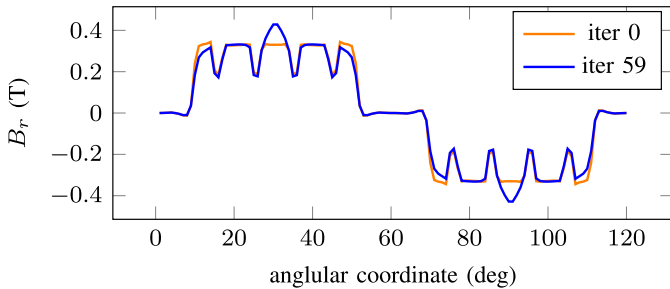


Fig. 11. Radial component  $B_r$  of the magnetic flux density in the air gap of the motor for the original design and for the optimized design after 59 iterations.

flux density in the air gap of the original and optimized design are shown in Figs. 10 and 11, respectively. The CAD description of the original and optimized machine geometries is also available as an IGES file [33]. The optimization leads to a very slight weakening of the torque. At full load, i.e., an excitation current with effective value  $I_{\text{eff}} = 10.6$  A, the original design has a torque of  $\tau_{\text{iter0}} = 11.62$  Nm. The torque of the optimized design is  $\tau_{\text{iter59}} = 11.34$  Nm. To investigate the impact of saturation on the results, the material of the rotor is modeled in JMAG by the nonlinear material curve M530-50 A for both, the original and the optimized geometry. The results for the THD of the EMF can be seen in Fig. 8 and Table I where still a reduction of 68 %



Fig. 12. Results of shape optimization (8)–(9) under full load condition. The shape of the rotor was optimized, minimizing the total harmonic distortion with the physical constraint (29) maintaining the average torque. Shape and position of the permanent magnet was fixed.

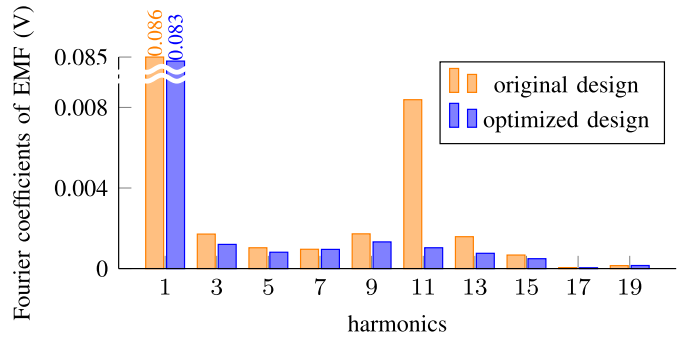


Fig. 13. Fourier coefficients of the electromotive force for the original design and for the optimized design after 59 iterations considering nonlinear material laws in stator and rotor core (i.e. electrical steel M530-50 A), calculated using JMAG.

is achieved. The comparison of the Fourier coefficients of the electromotive force for the original and the optimized machine considering nonlinear material laws is depicted in Fig. 13. Considering the saturation at partial load of 30 %, the torque is slightly reduced from  $\tau_{\text{iter0}} = 1.95$  Nm (original design) to  $\tau_{\text{iter59}} = 1.90$  Nm (optimized design). The THD of the EMF is reduced by 26 % from  $\text{THD}_{\text{iter0}} = 0.132$  (original design) to  $\text{THD}_{\text{iter59}} = 0.098$  (optimized design). In conclusion, the consideration of fully nonlinear material laws increases the THD but the optimization using the linear model is still very effective.

## VIII. CONCLUSION

This paper has proposed a freeform shape optimization methodology based on isogeometric analysis. The method has been applied to optimize the shape of an interior permanent magnet synchronous machine. The optimized geometry exhibits a significantly reduced total harmonic distortion, i.e., up to a factor of four. It has been demonstrated that the spline-based geometry representation allows easy integration into existing workflows using proprietary software.

In future works the optimization method will be extended to nonlinear material laws, different load scenarios and robustness, i.e., minimizing the effect small deviations from the nominal design have on the behavior of the machine. Furthermore, the method shall be applied to three-dimensional machine models and extended to take into account nonlinear material relations.

## ACKNOWLEDGMENT

The authors would like to thank C. Mellak, H. De Gerssem, Z. Bontinck and J. Corno for their help and the fruitful discussions.

## REFERENCES

- [1] T. J. R. Hughes, J. A. Cottrell, and Y. Bazilevs, "Isogeometric analysis: CAD, finite elements, NURBS, exact geometry and mesh refinement," *Comput. Methods Appl. Mech. Eng.*, vol. 194, pp. 4135–4195, 2005.
- [2] A. Buffa, G. Sangalli, and R. Vázquez, "Isogeometric analysis in electromagnetics: B-splines approximation," *Comput. Methods Appl. Mech. Eng.*, vol. 199, pp. 1143–1152, 2010.
- [3] Z. Bontinck *et al.*, "Recent advances of isogeometric analysis in computational electromagnetics," *ICS Newsletter* (International Compumag Society), vol. 3, Nov. 2017. [Online]. Available: <http://www.compumag.org/jsite/images/stories/newsletter>
- [4] J. Dölz, H. Harbrecht, S. Kurz, S. Schöps, and F. Wolf, "A fast isogeometric BEM for the three dimensional Laplace- and Helmholtz problems," *Comput. Methods Appl. Mech. Eng.*, vol. 330, pp. 83–101, Mar. 2018.
- [5] P. Gangl, U. Langer, A. Mantzaflaris, and R. Schneckleitner, "Isogeometric simulation and shape optimization with applications to electrical machines," in *Scientific Computing in Electrical Engineering (SCEE 2018)*, G. Nicosia and V. Romano, Eds., vol. 32. Springer International Publishing, 2020, pp. 35–44.
- [6] P. Di Barba, *Multiobjective Shape Design in Electricity and Magnetism, Ser. Lecture Notes in Electrical Engineering*. Netherlands: Springer, 2010.
- [7] Y. Duan and D. M. Ionel, "A review of recent developments in electrical machine design optimization methods with a permanent-magnet synchronous motor benchmark study," *IEEE Trans. Ind. Appl.*, vol. 49, no. 3, pp. 1268–1275, May 2013.
- [8] S. Russenschuck, "Mathematical optimization techniques for the design of permanent magnet synchronous machines based on numerical field calculation," *IEEE Trans. Mag.*, vol. 26, no. 2, pp. 638–641, Mar. 1990.
- [9] K. Weeber and S. R. H. Hoole, "Geometric parametrization and constrained optimization techniques in the design of salient pole synchronous machines," *IEEE Trans. Mag.*, vol. 28, no. 4, pp. 1948–1960, Jul. 1992.
- [10] N. Takorabet, B. Laporte, and G. Vinsard, "On the optimization of linear induction devices," *Elect. Eng.*, vol. 80, pp. 221–226, 1997.
- [11] K. Hameyer and M. Kasper, "Shape Optimization of a Fractional Horse-Power DC-Motor by Stochastic Methods," in *Computer Aided Optimum Design of Structures III: Optimization of Structural Systems and Applications*, S. Hernandez and C. Brebbia, Eds., 1993, pp. 15–30.
- [12] C. L. Lok, B. Vengadaesvaran, and S. Ramesh, "Implementation of hybrid pattern search-genetic algorithm into optimizing axial-flux permanent magnet coreless generator (AFPMG)," *Elect. Eng.*, vol. 99, pp. 751–761, 2017.
- [13] C. Ma and L. Qu, "Multiobjective optimization of switched reluctance motors based on design of experiments and particle swarm optimization," *IEEE Trans. Energy Convers.*, vol. 30, no. 3, pp. 1144–1153, Sep. 2015.
- [14] U. Baumgartner, C. Magele, and W. Renhart, "Pareto optimality and particle swarm optimization," *IEEE Trans. Magn.*, vol. 40, no. 2, pp. 1172–1175, Mar. 2004.
- [15] S. L. Ho, S. Yang, L. E. W. C. Ni Guangzheng, and H. C. Wong, "A particle swarm optimization-based method for multiobjective design optimizations," *IEEE Trans. Mag.*, vol. 41, no. 5, pp. 1756–1759, May 2005.
- [16] B. N. Cassimere and S. D. Sudhoff, "Population-based design of surface-mounted permanent-magnet synchronous machines," *IEEE Trans. Energy Convers.*, vol. 24, no. 2, pp. 338–346, Jun. 2009.
- [17] M. L. Bash and S. D. Pekarek, "Modeling of salient-pole wound-rotor synchronous machines for population-based design," *IEEE Trans. Energy Convers.*, vol. 26, no. 2, pp. 381–392, Jun. 2011.
- [18] G. Y. Sizov, P. Zhang, D. M. Ionel, N. A. O. Demerdash, and M. Rosu, "Automated multi-objective design optimization of PM AC machines using computationally efficient FEA and differential evolution," *IEEE Trans. Ind. Appl.*, vol. 49, no. 5, pp. 2086–2096, Sep. 2013.
- [19] B. D. S. G. Vidanalage, M. S. Toulabi, and S. Filizadeh, "Multimodal design optimization of V-shaped magnet IPM synchronous machines," *IEEE Trans. Energy Convers.*, vol. 33, no. 3, pp. 1547–1556, Sep. 2018.
- [20] M. De Martin, F. Luise, S. Pieri, A. Tessarolo, and C. Poloni, "Numerical multi-objective optimization of a squirrel cage induction motor for industrial application," in *Proc. Intl Aegean Conf. Elect. Machines Power Electron. (ACEMP), Intl Conf. Optim. Elect. Electron. Equip. (OPTIM) Intl Symp. Adv. Electromechanical Motion Syst. (ELECTROMOTION)*, 2015, pp. 170–175.
- [21] S. S. R. Bonthu, M. T. B. Tarek, and S. Choi, "Optimal torque ripple reduction technique for outer rotor permanent magnet synchronous reluctance motors," *IEEE Trans. Energy Convers.*, vol. 33, no. 3, pp. 1184–1192, Sep. 2018.
- [22] Z. Bontinck, J. Corno, S. Schöps, and H. De Gerssem, "Isogeometric analysis and harmonic stator-rotor coupling for simulating electric machines," *Comput. Methods Appl. Mech. Eng.*, vol. 334, pp. 40–55, 2018.
- [23] S. Schöps, H. De Gerssem, and T. Weiland, "Winding functions in transient magnetoquasistatic field-circuit coupled simulations," *COMPEL*, vol. 32, no. 6, pp. 2063–2083, Sep. 2013.
- [24] P. Gangl, U. Langer, A. Laurain, H. Meftahi, and K. Sturm, "Shape optimization of an electric motor subject to nonlinear magnetostatics," *SIAM J. Sci. Comput.*, vol. 37, no. 6, pp. B 1002–B1025, 2015.
- [25] H. Egger, M. Harutyunyan, M. Merkel, and S. Schöps, "On the stability of harmonic mortar methods with application to electric machines," in *Scientific Computing in Electrical Engineering (SCEE 2020)* (Mathematics in Industry), M. van Beurden, N. Budko, and W. Schilders, Eds., Berlin, Germany: Springer, 2021.
- [26] L. Piegl and W. Tiller, *The NURBS Book*, 2nd ed., Berlin Heidelberg, Germany: Springer, 1997.
- [27] A. Buffa, R. H. Vázquez, G. Sangalli, and L. B. da Veiga, "Approximation estimates for isogeometric spaces in multipatch geometries," *Numer. Methods Partial Differ. Equ.*, vol. 31, no. 2, pp. 422–438, 2015.
- [28] J. Nocedal and S. J. Wright, *Numerical optimization*, (Ser. Springer Series in Operations Research and Financial Engineering) 2nd ed., New York, NY, USA: Springer-Verlag.
- [29] V. Schulz and M. Siebenborn, "Computational comparison of surface metrics for pde constrained shape optimization," *Comput. Methods Appl. Math.*, vol. 16, no. 3, pp. 485–496, Jul. 2016.
- [30] U. Pahnner, "A general design tool for the numerical optimisation of electromagnetic energy transducers," Ph.D. dissertation, KU Leuven, Leuven, Belgium, May 1998.
- [31] Z. Bontinck, "Simulation and robust optimization for electric devices with uncertainties," Ph.D. dissertation, Technische Universität Darmstadt, 2018.
- [32] C. de Falco, A. Reali, and R. Vázquez, "GeoPDEs: A research tool for isogeometric analysis of PDEs," *Adv. Eng. Softw.*, vol. 42, pp. 1020–1034, 2011.
- [33] M. Merkel, P. Gangl, and S. Schöps, "Results of the shape optimization of rotating electric machines using isogeometric analysis," Feb. 2020. [Online]. Available: <https://doi.org/10.5281/zenodo.3688478>